The Moist Boundary Layer under a Mid-latitude Weather System

I. A. Boutle · **R. J. Beare** · **S. E. Belcher** ·
A. R. Brown · **R. S. Plant**

Abstract Mid-latitude weather systems are key contributors to the transport of atmospheric water vapour, but less is known about the role of the boundary layer in this transport. We expand a conceptual model of dry boundary-layer structure under synoptic systems to include moist processes, using idealised simulations of cyclone waves to investigate the three-way interaction between the boundary layer, atmospheric moisture and large-scale dynamics. Forced by large-scale thermal advection, boundary-layer structures develop over large areas, analogous to the daytime convective boundary layer, the nocturnal stable boundary layer and transitional regimes between these extremes.

A budgeting technique demonstrates the key role of boundary-layer processes in the transport of moisture. Moisture is evaporated from the ocean behind the cold front and in the high-pressure part of the wave, and transported large distances within the boundary layer into the footprint of the warm-conveyor belt. The warm-conveyor belt forms one of the two main processes of boundary-layer ventilation, with shallow cumulus convection being of similar importance.

Keywords Cyclone waves · Moisture cycle · Synoptically-forced boundary layer

I. A. Boutle · S. E. Belcher · R. S. Plant
Department of Meteorology, University of Reading, PO Box 243, Reading, RG6 6BB, UK

Present address: I. A. Boutle
Met Office, FitzRoy Road, Exeter, EX1 3PB, UK
E-mail: ian.boutle@metoffice.gov.uk

R. J. Beare
School of Engineering, Computing and Mathematics, University of Exeter, Exeter, EX4 4QF, UK

A. R. Brown
Met Office, FitzRoy Road, Exeter, EX1 3PB, UK

1 Introduction

The atmospheric boundary layers is typically thought of under two broad categories: (i) a single-column boundary layer forced by the diurnal cycle over a land surface, where the growth and characteristics are determined by the surface energy balance; and, (ii) a two-dimensional internal boundary layer, growing downwind of a change in surface characteristics (e.g. a rural to urban boundary). However, synoptic-scale atmospheric phenomena also control the structure of the boundary layer in complex, three-dimensional ways. This has been highlighted recently by Sinclair et al. (2010) through idealised, dry, simulations of mid-latitude cyclone waves. Strong surface heat fluxes can result from the large-scale thermal advection of heat within such synoptic systems, driving the boundary-layer structure. This produces large areas that are consistent with classical stable and unstable boundary-layer regimes, but which undergo transitions as the system evolves. Sinclair et al.'s (2010) results provide a simple conceptual model of dry boundary-layer structure on synoptic scales, but raise the question how their results can be extended in the presence of a moist atmosphere.

Previous studies of boundary layers under synoptic systems have tended to be observationally based. The Joint Air-Sea Interaction Project (JASIN) was designed to observe the physical processes causing mixing in oceanic and marine boundary layers, and quantify aspects of the heat and momentum budgets in mid-latitude regions. Businger and Charnock (1983) discussed the large-scale boundary-layer structure, commenting how the observed cloud layer, typically containing cumulus and stratocumulus, was "apparently maintained by processes occurring on scales greater than 50 km" (Businger and Charnock, 1983, p. 446). They also noted that subtle differences in the boundary-layer structure can lead to large differences in the formation and dissipation of clouds, demonstrating how processes acting over a wide range of spatial and temporal scales are responsible for the observed boundary-layer structure and evolution.

Other observational studies have tended to focus in detail on one aspect of the interaction between the boundary layer and synoptic scale. Taylor and Guymer (1983) provided a detailed description of the interaction of a warm front with the boundary layer, whilst a similar perspective on the boundary-layer structure near a cold front is provided by Berger and Friehe (1995). The latter study formed part of the Experiment on Rapidly Intensifying Cyclones over the Atlantic (ERICA), for which Neiman et al. (1990) also provide a detailed description of surface sensible and latent heat fluxes under a rapidly-intensifying cyclone, along with the effect of these fluxes on the cyclone's evolution.

The problem with observational studies is that most cyclogenesis events occur over the open ocean, where even during intensive observational campaigns, the coverage and the horizontal and vertical resolution of data can be low, meaning that the larger-scale structures are not well observed. Therefore a computational modelling approach has been used (e.g. Kuo et al., 1991; Levy, 1989) to ascertain the detailed cyclone–boundary-layer interaction. However, initial conditions and model uncertainty can lead to differing results from modelling studies, even when simulating the same cyclone. Therefore, we have chosen to pursue an idealised modelling approach such as that taken by Nuss (1989) and Becker et al. (1996). This allows us

to investigate the boundary-layer response to a generic and well-defined large-scale perturbation, as well as any feedback processes involved, without more complex atmospheric flows distorting the synoptic-scale evolution.

Mid-latitude cyclones have the capacity to induce torrential rains and damaging winds to large, densely populated areas, making accurate forecasts crucial in planning for these potentially life-threatening events. There have been many studies of idealised, dry, frictionless cyclogenesis (e.g. Eady, 1949; Thorncroft et al., 1993) and this process is now thought to be well-understood. Emanuel et al. (1987) and others have proposed modifications to these conceptual models that account for the presence of moisture in the atmosphere, and recently Adamson et al. (2006), Beare (2007) and Boutle et al. (2007) have discussed a new conceptual model of how boundary-layer friction affects dry cyclogenesis.

Idealised cyclone-wave life cycles (e.g. Thorncroft et al., 1993) have been used to study the structure, evolution and energetics of cyclone-anticyclone systems and their role in the poleward transport of heat and momentum. However, due to the need for accurate parameterisations of convection, cloud microphysics and precipitation, studies of moist cyclone-wave life cycles are relatively few in number. Gutowski et al. (1992) and Pavan et al. (1999) describe large-scale features, energetics and moisture transport in cyclone waves with relatively simple moisture parameterisations. Furthermore, since they focus on the large-scale development, they only include a single-layer parameterisation of surface drag and heat/moisture exchange, and this is done for completeness rather than to study the boundary layer. Gutowski and Jiang (1998) use improved parameterisations to study the effects of surface fluxes on the interaction between shallow cumulus and cyclone waves. Their results demonstrate how cyclone waves are important in redistributing moisture within the free troposphere, but do not fully investigate how crucial the boundary layer is in this process. Field and Wood (2007) used a composite of satellite-observed cyclones to demonstrate a strong correlation between moisture convergence in the boundary layer and cyclone rainfall rate, but what are the physical processes occurring in the boundary layer that form and maintain this moisture source?

In this paper we have chosen to investigate the synoptic-scale boundary layer in idealised cyclone-wave simulations with almost full physics. The aim of the work is to determine the structure of the boundary layer under a developing cyclone wave and how the boundary layer evolves to this state during a cyclogenesis event. We aim to ascertain how the presence of moisture modifies conceptual models of dry boundary-layer structure, and whether a conceptual model of boundary-layer moisture regimes can be developed. We also aim to assess quantitatively the role of the synoptic boundary layer in redistributing moisture in the horizontal and venting it into the free troposphere. In Section 2 we discuss the model set-up and initialisation used, and describe the large-scale evolution in Section 3. In Section 4 we discuss the structure and evolution of the boundary layer in a qualitative manner, considering how to classify moisture regimes in Section 5. Finally, we add a quantitative description with budgeting techniques in Section 6 and conclude in Section 7.

2 Model Description and Initialisation

We have chosen to investigate the boundary-layer structure under a life cycle similar to that denoted LC1 by Thorncroft et al. (1993). This idealised cyclone-wave structure captures the main features of extratropical cyclogenesis, and the effect of the boundary layer in dry LC1 simulations has been discussed previously by Adamson et al. (2006) and Sinclair et al. (2010). We use an idealised configuration of the UK Met Office Unified Model (MetUM, version 6.1), which has a full range of physical parameterisations (see Martin et al. (2006) for a recent review), the most important for our work being the treatment of moist boundary layers. Between the surface and lowest model level (located at 10 m), Monin-Obukhov similarity theory is used to calculate the surface fluxes, using the formulation described in Beljaars and Holtslag (1991). The above-surface fluxes, calculated over the remaining 12 levels below 3 km, are parameterised using a first-order mixing length scheme. The stable boundary-layer formulation is described in Beare and MacVean (2004), with long-tailed stability functions used here. In unstable layers, a K-profile closure is used with a counter-gradient component for the sensible heat flux, as described in Lock et al. (2000). An explicit entrainment parameterisation is used at the top of well-mixed layers and stratocumulus clouds. Cumulus cloud transports are performed by a mass-flux scheme.

The MetUM was configured on a Cartesian limited area domain ((x, y, z) co-ordinates with z normal to the Earth's surface), with the Coriolis parameter kept constant at its 45°N value. East-west periodic boundary conditions and fixed north and south boundaries were applied, giving a channel flow that allows the cyclone wave to develop for many days uninhibited by horizontal boundary conditions. The domain was 60° longitude by 80° latitude, with a resolution of 0.4° in the horizontal and 38 staggered vertical levels (similar to the current global forecast operational resolution). The large meridional extent was chosen so that the north-south boundaries have no effect on the simulated cyclone, whilst the use of Cartesian co-ordinates makes our cyclone-wave simulation slightly different to the LC1 simulation discussed in Sinclair et al. (2010), but no less realistic. The differences between Cartesian f-plane simulations and spherical simulations are well documented in the literature (e.g. Balasubramanian and Garner, 1997; Wernli et al., 1998), with the major difference being that the cyclonic branches of the large-scale flow are more prominent in Cartesian simulations. Similar results to the Cartesian simulations can be obtained by the use of spherical co-ordinates with the addition of a small cyclonic shear to the basic state.

For simplicity the radiation scheme was switched off and the model was run entirely over a sea-surface. This allows us to isolate the boundary-layer response to forcing from the synoptic scale only, rather than trying to disentangle the effect of different forcing mechanisms, such as a diurnal cycle or cloud-radiation interactions, on the boundary-layer evolution. The consequences of this simplification will be discussed further in Section 7.

The initial state was a zonally-oriented jet (Figure 1a), defined in the same way as Polvani and Esler (2007) to represent the climatology of the Northern Hemisphere wintertime storm track. A temperature profile is then calculated in thermal-wind balance with the jet, and a pressure profile in hydrostatic balance with this. The model

is run for several timesteps to allow the initial profiles to adjust to a non-hydrostatic balance consistent with the equation set of the MetUM. The sea-surface temperature is fixed equal to the initial temperature of the lowest model level, and kept constant throughout the simulation.
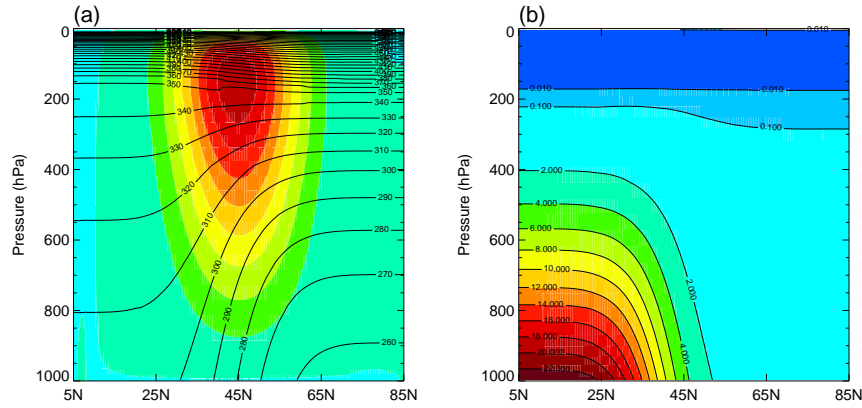

Fig. 1 (a) Initial zonal winds (colour shading, interval 5 m s^{-1}, maximum 45 m s^{-1}) and potential temperature (black contours, interval 10 K). (b) Initial zonal-mean specific humidity distribution (colour shading, interval 2 g kg^{-1}).

We wish to create an analytic profile of the atmospheric moisture distribution that is representative of the wintertime storm track climatology. We define this in terms of relative humidity (RH) so that the actual moisture content will depend on the temperature profile. The first constraint is that RH must decrease as z increases, and we define the z dependence of RH by

$$RH(y, z) = \begin{cases} 80\% \left(1 - 0.9R(y)(z/z_T)^{5/4}\right) & z < z_T \\ 5\% & z > z_T \end{cases}, \tag{1}$$

where $z_T = 12$ km is a moisture scale-height, designed to give a sharp gradient in the region of the tropopause, and $R(y)$ is defined below. The second constraint is that most moisture is contained near the equator, decreasing across the jet region. For simplicity, we choose a linear decrease of moisture in the y direction as follows:

$$R(y) = \begin{cases} 1 & y < 25°\text{N} \\ 0.5 & y > 65°\text{N} \\ 1 - 0.5\left(\frac{y-25}{40}\right) & 25°\text{N} < y < 65°\text{N} \end{cases}. \tag{2}$$

When combined with our temperature profile, this produces the specific humidity profile shown in Figure 1b. The profile is chosen so that the specific humidity matches closely the profile used by Gutowski et al. (1992) (their Figure 1b), who approximate the climatological Northern Hemisphere winter zonal-mean state. Within the

$20 - 70°$N latitude band, the relative humidity profile also matches Figure 2 of Pavan et al. (1999), which presents the long-term mean of zonal-mean wintertime RH from re-analysis data. This moisture distribution therefore represents a good match to observed atmospheric profiles. Tests were performed that modified the RH profile defined in Equation 1 to different, but equally plausible, states. The resulting simulations were qualitatively similar, demonstrating that the results to be presented below are not overly sensitive to this choice of initial condition.

The initial zonal jet in Figure 1a is baroclinically unstable, meaning that it is unstable to small wave perturbations. These instabilities are called "cyclone waves" (Eady, 1949) as they consist of an alternating series of high and low pressure systems growing in time. The cyclone wave derives its energy from the reservoir of potential energy of the north-south potential temperature gradient shown in Figure 1a. We follow the method of Polvani and Esler (2007) to choose our small (maximum 1 K) wavenumber 6 perturbation to the potential temperature field.

3 Cyclone-Wave Evolution

Figure 2 shows the time evolution of minimum sea-level pressure and eddy kinetic energy (EKE), two measures of cyclone-wave intensity. EKE is half the volume-averaged squared departure of the horizontal winds (u, v) from their zonal-mean state. The two dry simulations demonstrate that the inclusion of the boundary-layer
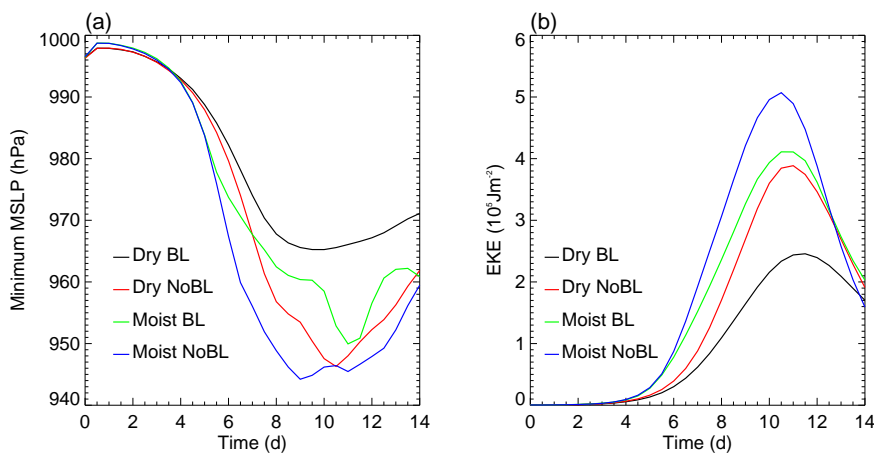

Fig. 2 Time series of (a) minimum sea-level pressure and (b) eddy kinetic energy, for four experiments: dry dynamics with the boundary-layer scheme active (black line), dry dynamics without the boundary-layer scheme (red), moist dynamics with the boundary-layer scheme active (green) and moist dynamics without the boundary-layer scheme (blue).

scheme, allowing surface momentum and heat exchange and near surface mixing, damps the wave's energetics and leads to a shallower cyclone. The two moist simulations demonstrate that the presence of a moist atmosphere leads to a more energetic

system with a deeper central pressure. This enhanced intensification can be understood qualitatively by considering a simple, frictionless model of tropospheric ascent forcing vortex stretching and spin-up of the cyclone. In the presence of moisture, latent heat is released in ascending regions, enhancing the ascent and so producing further spin-up.

It is also clear that the different physical processes start to have an effect on the system evolution after differing time scales. The moist runs start to diverge from the dry runs after ≈ 4 days, with the boundary layer starting to affect the development after ≈ 6 days. All experiments reach their maximum intensity between days 9 and 11, before starting to decay. The simulation with both moisture and the boundary-layer scheme included, denoted as "Moist BL", will be the focus of the remainder of this paper. We will also focus on the main growth stage of the system, up to day 10, and will not discuss the localised re-intensification shown between days 10 and 12 of this run. This is caused by latent heat release forcing a localised spin-up near the surface, but the feature is not large-scale as it does not appear in the EKE, and so is of little importance when considering the evolution of the whole system.

Figure 3 shows the spatial structure of the surface pressure, fronts, cloud fraction and precipitation rate on days 7 and 9 of the Moist BL simulation. It shows many fea-
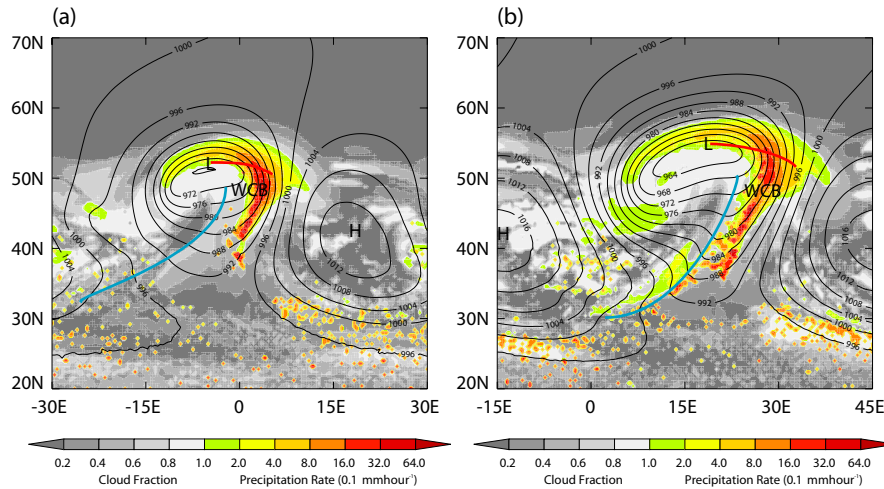

Fig. 3 Cloud fraction (shaded) and precipitation rate (coloured), with pressure at mean sea-level (contoured, interval 4 hPa) at (a) day 7 and (b) day 9. Red and blue lines denote the warm and cold fronts respectively and the letters "WCB" denote the location of the warm-conveyor belt.

tures of a classical mid-latitude weather system, such as the main precipitation band in the warm-conveyor belt (WCB) to the east and south-east of the low centre, marked on Figure 3. The WCB is the main poleward airflow in a mid-latitude cyclone, moving large amounts of warm, moist air polewards. The WCB runs ahead of the cold front and ascends over the warm front, splitting into two branches, one wrapping cyclonically around the north of the low centre, and the other wrapping anti-cyclonically east towards the high-pressure (Browning, 1990). The WCB ascends from within the

boundary layer up to $\approx$ 7 km, moving large amounts of moisture that contribute to its associated clouds and precipitation. The WCB tends to deliver the majority of a cyclone's precipitation, and the extent of the main precipitation band in Figure 3 identifies the spatial extent of the WCB. There is also some dry, cloud free air noticeable directly south of the low centre, immediately behind the cold front. This is associated with the dry intrusion, a large-scale descending branch of cold, dry air. Further behind the cold front and to the west of the cyclone centre, low-level cloud (tops at $\approx$ 3 km) is formed within the cold-air outbreak. As cold air flows quickly from the north between the cyclone and anticyclone, it flows over a much warmer sea surface, leading to the formation of stratocumulus and shallow cumulus. The shallow cumulus extends towards the centre of the anticyclone, but disappears to leave cloud-free air in the very centre of the high-pressure where there are light winds and little thermal advection. To the very south of the domain there is some scattered convective rainfall. By day 9 most of this lies along the trailing front to the south of the high, where there is some horizontal convergence. To the very north of the domain the air is cold and dry and therefore cloud free with no precipitation.

4 Boundary-Layer Structure

The structure and evolution of the boundary layer under a cyclone wave will now be discussed, demonstrating how large-scale processes form and maintain the appearance of the boundary layer as the cyclone wave intensifies.

4.1 Surface Fluxes

Surface fluxes are calculated in the model by bulk relations, adjusted for stability using Monin-Obukhov theory, assuming that the lowest model level lies within the surface layer. Scalar fluxes are given by

$$H_s = \rho C_p C_H |\mathbf{v}_1|(\theta_s - \theta_1), \tag{3}$$

$$\lambda E_s = \rho \lambda C_H |\mathbf{v}_1|(q_{\mathrm{sat}}(\theta_s) - q_1), \tag{4}$$

where H_s is the surface sensible heat-flux, ρ is the density of air, C_p is the specific heat capacity of air at constant pressure, C_H is the transfer coefficient for heat, $|\mathbf{v}_1|$ is the wind speed on the lowest model level, $\theta_s - \theta_1$ is the difference between the surface and lowest model level potential temperature, λ is the latent heat of vaporisation, E_s is the evaporation rate and $q_{\mathrm{sat}}(\theta_s)$ is the saturation specific humidity of the surface temperature. The surface fluxes are shown in Figure 4 after 7 days and show broadly similar patterns. Within the warm-conveyor belt region there are negative fluxes of both sensible and latent heat: warm, moist air moves over the cooler sea-surface, losing heat and becoming super-saturated with respect to the surface, forcing the moisture to condense out in a similar manner to dew formation over land.

The main regions of positive heat fluxes are behind the cold front, extending into the high pressure part of the wave. It is noticeable that the maximum values for sensible and latent heat are not coincident. The greatest sensible heat flux can be seen
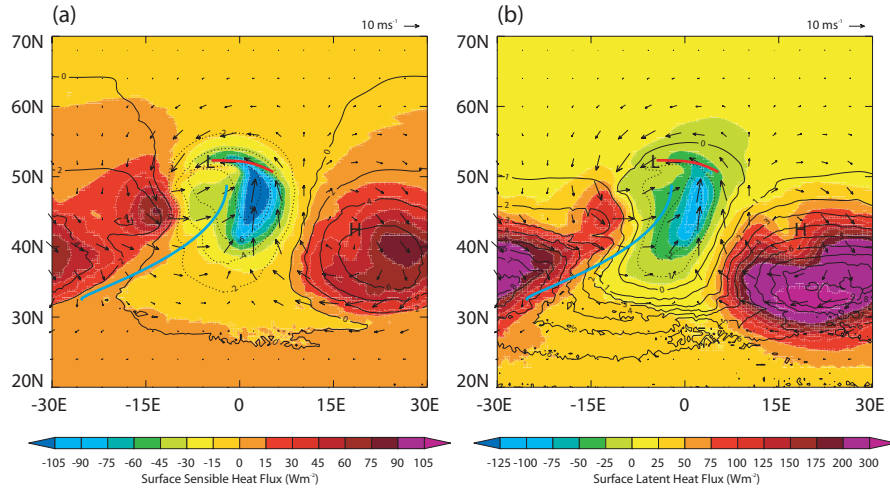
Fig. 4 Surface fluxes at day 7 showing (a) sensible heat (coloured) with $\theta_s - \theta_1$ (contoured, interval 2 K, negative values dotted), and (b) latent heat (coloured) with $q_{\text{sat}}(\theta_s) - q_1$ (contoured, interval 1 g kg^{-1}, negative values dotted). Wind vectors for every tenth gridpoint at the lowest model level (10 m) are over-plotted on both panels. The L and H are added to mark the low and high pressure centres.

to the east of the high centre, where there is the greatest thermal advection of cold air over the warm sea surface, giving the greatest contrast in temperature. However, the latent heat flux is greatest where the greatest saturation deficit occurs, which is to the south of the high centre, because the air and sea-surface temperatures (SSTs) are both higher here, and hence the saturation vapour pressure is larger. The pattern of sensible heat flux is similar to that in Sinclair et al. (2010) for dry cyclone-wave simulations, and to that in Brown et al. (2008) for a real case-study. The main difference from Sinclair et al. (2010) occurs in the secondary maximum of sensible (and latent) heat to the south-west of the low centre ($-15°$E, $45°$N). This is due to a low-level jet that wraps around the cyclone centre, generating stronger wind speeds in this location. Coupled with the stronger advection of cold (dry) air over a higher SST, this gives rise to the secondary maximum. This feature is caused by a combination of differences in the cyclone dynamics and the large-scale effect of moisture intensifying the system. The range of values of surface fluxes in the simulation are similar to those reported in observational studies (e.g. Neiman et al., 1990; Kuo et al., 1991), and previous idealised studies (e.g. Nuss, 1989).

Within the surface layer, the stress is given by the bulk aerodynamic relation, and its distribution and magnitude can be most easily seen in terms of the friction velocity

$$u_* = \left(\frac{|\tau|}{\rho}\right)^{1/2} = C_D^{1/2}|\mathbf{v}_1|, \tag{5}$$

where τ is the surface stress and C_D is the drag coefficient. The friction velocity is shown in Figure 5a and shows two distinct regions of enhanced momentum transfer. The first is in the WCB region, coincident with the negative scalar fluxes, whilst the second is in the region of the low-level jet, coincident with the secondary maxima

10

of the scalar fluxes. Boutle et al. (2007) discuss how momentum transfer in these two regions can affect the large-scale development of the cyclone. There is also enhanced momentum transfer to the east and south of the anticyclone associated with air circulating around the high pressure system.
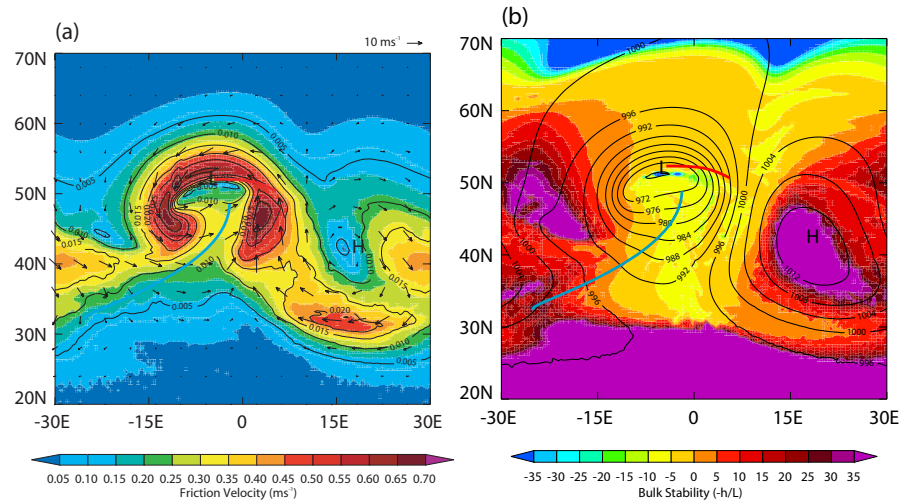

Fig. 5 (a) Friction velocity (coloured) with C_D (contoured, interval 0.005) and wind vectors every tenth gridpoint at the lowest model level over-plotted. (b) Bulk stability ($-h/L$, coloured) with pressure at mean sea-level (contoured, interval 4 hPa), at day 7.

4.2 Boundary-layer Structure

The bulk stability of the boundary layer is often considered in terms of the dimensionless quantity $-h/L$, where h is the boundary-layer depth (as diagnosed by the MetUM, see Section 6.1 for further details) and L is the Obukhov length. This stability measure is shown in Figure 5b, indicating that the boundary layer is only weakly stable in the warm-conveyor belt region, with $-h/L$ values between -5 and -10. This explains the large values of scalar and momentum fluxes in this region: although the boundary layer is stable, there is still significant turbulent mixing allowing large surface-flux exchanges. Within the high pressure region, the boundary layer is most unstable in the region of highest pressure, but, as in Sinclair et al. (2010), this is not coincident with the largest surface fluxes due to the very low wind speeds here. To the very south of the domain, the boundary layer is very unstable, due to the high moisture content and high SSTs at this latitude, and conversely to the very north of the domain the boundary layer is very stable, due to the low moisture content and low SSTs.

Figure 5b showed how the boundary-layer stability, driven mainly by the surface buoyancy flux, can be broadly characterised as being stable within the cyclonic region

and unstable within the anticyclonic region. However, in a simulation with moisture, the presence of cloud has a significant effect on the boundary-layer structure and evolution.

Classical types of boundary-layer development can be observed within different areas of the system, although the forcing is through large-scale thermal advection in this case, rather than through diurnal heating and cooling. In regions of positive surface fluxes, a convective boundary layer grows as the wave intensifies. Initially, a single mixed layer is formed, with capping cloud created when this mixed layer grows higher than the lifting condensation level. By day 4 this stratocumulus becomes decoupled from the surface in some places and shallow cumulus convection may be initiated beneath it. By day 7 the shallow convection has become strong enough in some places to produce a cumulus-capped layer extending up to ≈ 3 km. Figure 6a shows a vertical profile through such a boundary layer at this stage of evolution. There is a moist, well-mixed layer extending up to ≈ 1 km, over which the turbulent moisture flux ($E = \rho \overline{w'q'}$) decreases from its surface value down to zero at the cloud base. Above this the atmosphere is conditionally unstable and moist convection acts to mix the moisture profile throughout the cloud depth. The liquid water content of the shallow cumulus is also shown in the figure.
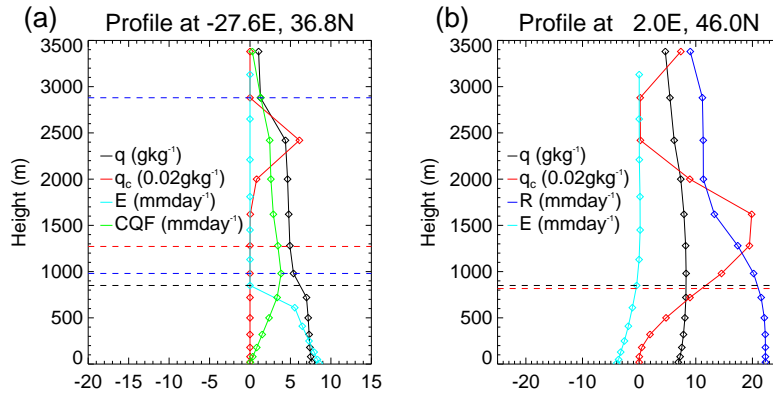

Fig. 6 Profiles of specific humidity (q), cloud water content (q_c), turbulent moisture flux (E), convective moisture flux (CQF) and precipitation rate (R) at day 7, for: (a) the cumulus-capped post-frontal boundary layer; and, (b) the stable WCB boundary layer. The abscissa units for each profile are shown on the panels. The horizontal black dashed lines denote the MetUM diagnosed boundary-layer depth, while blue dashed lines denote the extent of convective cloud and red dashed lines denote the boundary-layer depth as diagnosed from the method of Troen and Mahrt (1986).

Within the warm-conveyor belt region, the boundary layer shows some of the classical features of a nocturnal boundary layer. Dew formation on the surface has already been mentioned in Section 4.1, but above the surface, the air becomes supersaturated and moisture is forced to condense out as low-level cloud or fog. The boundary-layer structure here is complicated by large-scale processes that are acting in the lower troposphere. The large-scale ascent on the warm-conveyor belt and associated cloud and precipitation, in addition to strong wind shear, all contribute to

a large amount of mixing within a boundary layer that would be considered stable on buoyancy grounds. Figure 6b shows a vertical profile through this warm-conveyor belt region. The humidity profile remains well-mixed throughout a large layer of the atmosphere since moisture is being lost to the surface, but also mixed upwards within the cloud layer. Section 6.2 will discuss how large-scale advection is having an effect on the boundary-layer moisture distribution at this point. There are two distinct layers of cloud visible, one well above the boundary layer on the conveyor belt (> 3 km high) and another within the boundary layer ($\approx 500 - 2500$ m). The upper layer of cloud is precipitating, and this precipitation is enhanced by the lower layer of cloud.

It is also worth noting that the cyclone wave is constantly propagating eastwards, and so at any fixed point in space, the boundary layer will be undergoing transition between these stable and unstable regimes on a time scale of $3 - 4$ days.

5 Moisture Regimes

Thus far, boundary-layer regimes have only been considered in terms of stable or unstable boundary layers forced by the surface sensible heat flux. Whilst this classification is undoubtedly useful, it does not provide any information about the boundary-layer moisture structure. Mahrt (1991) attempted to classify regimes dependent on their stability and moisture availability, using the bulk stability ($-h/L$) and the Bowen ratio ($H_s/\lambda E_s$). The phase space of bulk stability and Bowen ratio is plotted in Figure 7a for the $30 - 60°$N latitude range. The figure shows three distinct regions of
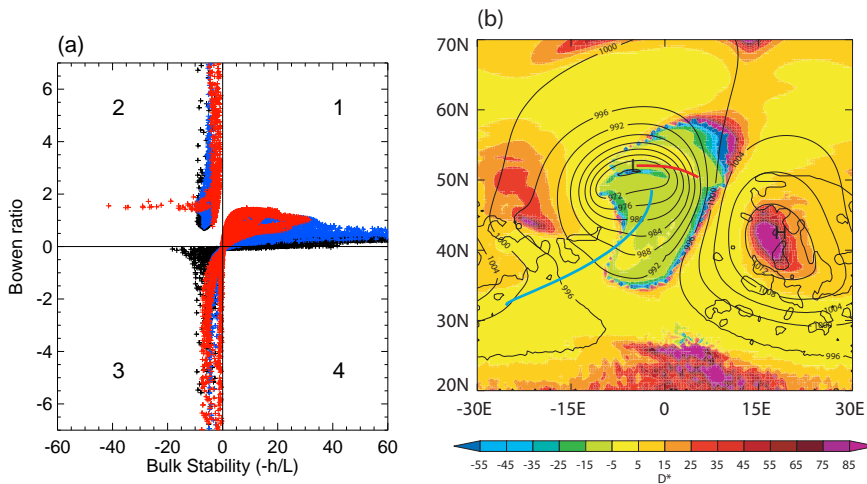

Fig. 7 (a) Bowen ratio and bulk stability phase space for the $30 - 60°$N latitude band (black, $30 - 40°$N; blue, $40 - 50°$N; red, $50 - 60°$N). The quadrants are labelled for ease of reference within the main text. (b) $D^* = (-h/L)(H_s/\lambda E_s)$ (coloured) with mean sea-level pressure (thin contours, interval 4 hPa) at day 7. Regions of cumulus-capped boundary layers are also marked, by thick lines.

interest. Quadrant 1 is a region of positive buoyancy with low Bowen ratio. This sig-

nifies a convective boundary layer where the latent heat flux exceeds the sensible heat flux, and corresponds to an area behind the cold front extending into the high pressure region. Moisture is freely available from the sea surface and the thermal advection of relatively cold air controls the stability. Within calm regions, near the anticyclonic centre, buoyancy dominates the turbulence, whilst in windy regions to the east of this centre there is also shear-generated turbulence.

Quadrant 2 corresponds to a weakly stable boundary layer with large Bowen ratio. Both the sensible and latent heat fluxes are negative, and this corresponds to the warm-conveyor belt area to the south-east of the low centre. As warm, moist air moves polewards over a colder sea surface, fluxes act to reduce both the heat and moisture content. The latent heat flux is limited since dew formation is only one of three possible processes that remove moisture from this air. As discussed in Section 4.2, the moisture can also condense out within the air to form low-level cloud or fog, whilst the large-scale ascent on the warm-conveyor belt can also ventilate moisture from the boundary layer into the troposphere. In contrast, the sensible heat flux can become very large because the loss of heat to the surface is the only way to cool the air. This gives rise to the large Bowen ratios observed in this regime.

The third region, in Quadrant 3, consists of a weakly stable boundary layer with negative Bowen ratio, implying a positive latent heat flux. This region represents a transitional regime between the two extreme cases discussed above. Figure 4 shows the relevant areas within the wave, where the boundary layer is only weakly stable on buoyancy grounds, but shear-induced turbulence from the low-level winds is sufficient to cause evaporation into the unsaturated boundary layer. In some places, values of both H_s and λE_s are small, however, which can result in large values of Bowen ratio where λE_s approaches zero more rapidly than H_s.

Mahrt (1991) considered two prototype moisture regimes: a boundary layer drying by entrainment from above, or one moistening due to surface fluxes. These were characterised in terms of the nondimensional quantity D^*, defined as

$$D^* = \left(-\frac{h}{L}\right) \frac{H_s}{\lambda E_s}. \tag{6}$$

Figure 7b shows this quantity at day 7 in the life cycles. D^* is largest when $-h/L$ is large and E_s is small, which corresponds to a convective boundary layer with little surface moisture flux. Under these conditions, the boundary layer is characterised by large eddies, which contribute to significant entrainment of dryer air from above, hence characterising the entrainment drying regime. Conversely, D^* is small and positive when $-h/L$ is small and E_s is large, corresponding to a weakly convective or shear-driven boundary layer with large surface evaporation. Here, the boundary layer is moistening from below with little entrainment of dryer air from above. Both these regimes can be seen in the post-frontal and anticyclonic areas of the wave, with large D^* coincident with the anticyclone's centre and small D^* to the east of this. It is also noticeable that small values of D^* match regions of cumulus convection, whereas large values of D^* are coincident with areas of a single mixed layer, consistent with the notion that entrainment drying of the boundary layer is inhibiting shallow convection and cloud formation.

The results presented here show that a third moisture regime is also required in this classification scheme, one defined by negative values of D^* and characterised by a stable boundary layer losing moisture to the surface via condensation. However, complex synoptic-scale airflows within this area of the cyclone wave could result in the boundary layer as a whole either drying or moistening, depending on the composition of the air converging into it. For this reason, we apply a budgeting technique in the next section to unravel the effects of the relevant airflows.

6 Boundary-Layer Budgets

6.1 Derivation of Moisture Budget

To determine the redistribution of moisture by the cyclone wave, we follow the boundary-layer budgeting techniques used by Sinclair et al. (2010), only instead of the total mass content of the boundary layer, we are interested in the total moisture content:

$$\int_A \int_0^h \rho q \, dz \, dA, \tag{7}$$

where $q = q_v + q_{cl} + q_{cf}$, q_v is the specific humidity, q_{cl} the cloud liquid water and q_{cf} is the cloud frozen water, and A is an arbitrary area to be integrated over.

In performing the budget evaluations, we define the boundary-layer depth (h) following the method of Troen and Mahrt (1986). This is essentially the basis of the MetUM diagnosis of h, using a parcel ascent to calculate the level of neutral buoyancy for surface-based convective thermals. However, for reasons of scheme implementation, the MetUM re-defines h equal to the cloud base in regions of shallow cumulus (see Figure 6a). This can lead to discontinuities in the MetUM diagnosis of h at the edge of cumulus regions, whereas the Troen and Mahrt (1986) diagnosis finds h within such a cumulus cloud layer, giving a boundary-layer depth that is continuous in space and so allowing calculation of its spatial derivatives. This choice of method also provides consistency and simplifies comparison with Sinclair et al.'s (2010) mass-budget results.

Reynolds averaging gives rise to the moisture equation

$$\frac{\partial}{\partial t}(\rho q) + \nabla.(\rho q \mathbf{u}) = -\frac{\partial}{\partial z}(\rho \overline{w'q'}) + \mathscr{S}, \tag{8}$$

where $\mathbf{u}$ is the full velocity vector (u, v, w), and $\mathscr{S}$ is a source or sink term from processes other than boundary-layer turbulence. The evolution of total moisture is obtained from a volume integral of Equation 8 (see Appendix for details), following which the integration over the arbitrary area A can ultimately be dropped to give

$$\frac{\partial}{\partial t}\widehat{\rho q} = \underbrace{(\rho q)_h \frac{\partial h}{\partial t}}_{1} \underbrace{-(\rho q)_h \mathbf{u}.\tilde{\mathbf{n}}}_{2} \underbrace{-\nabla_2.\widehat{\rho q \mathbf{v}}}_{3} \underbrace{-(\rho \overline{w'q'})_h + (\rho \overline{w'q'})_0}_{4} + \underbrace{\widehat{\mathscr{S}}}_{5}, \tag{9}$$

where $\widehat{\chi} = \int_0^h \chi \, dz$, ∇_2 is the horizontal gradient operator $(\frac{\partial}{\partial x}, \frac{\partial}{\partial y})$, $\mathbf{v}$ is the horizontal velocity vector (u, v) and $\tilde{\mathbf{n}}$ is a normal to the boundary-layer top. The subscript

h denotes a quantity evaluated at the boundary-layer top, or if there is a sharp inversion present, just below the inversion, since the entrainment flux is contained in term 4. Written in this form, term 1 represents the local change in boundary-layer depth, term 2 represents advection across the boundary-layer top, term 3 horizontal divergence within the boundary layer, term 4 the net vertical transport by boundary-layer turbulence and term 5 the net precipitation falling through the boundary layer. A caveat follows to this: shallow cumulus convection is also capable of moving moisture across the boundary-layer top, and if our model were fully convection resolving, then such transport would be included within term 2. However, shallow cumulus is parameterised within the model, separately from the boundary-layer parameterisation. Thus, there is an additional contribution to transport across the boundary-layer top, which we will consider separately and denote as $(\rho qw)_{\text{conv}}$.

6.2 Application of Moisture Budget

Numerical evaluation of the individual terms in Equation 9 produces a budget that is well-balanced. It also demonstrates that there is a negligible contribution from the fifth term, $\widehat{\mathscr{S}}$, since the precipitation is generally falling from above the boundary layer straight through to the surface, with little evaporation into the moist air beneath the warm-conveyor belt. There is also a negligible contribution from the entrainment flux, $\overline{w'q'}_h$, since entrainment is typically of dryer air that does not affect the total moisture content. At any fixed point in space, the overall rate of change of total moisture (left-hand side of Equation 9) is strongly linked to the rate of change of *h* (term 1), due to the eastwards progression of the cyclone wave forcing the transitioning boundary-layer structures discussed in Section 4. Therefore the moisture budget for these two terms appears very similar to the mass budget discussed in Sinclair et al. (2010). Moisture is gained as the boundary layer grows with the passage of the cold front, and is lost as the boundary layer shrinks with the approach of the stable WCB region. The other terms in the budget (2, 3, 4 and $(\rho qw)_{\text{conv}}$) provide insight into the system-relative moisture flows and low-level water cycle, and these are shown in Figure 8.

As moisture is evaporated from the sea surface behind the cold front and in the high pressure regions (Figure 8c), horizontal divergence forced by boundary-layer drag transports moisture within the boundary layer away from this region. This maintains the saturation deficit, allowing strong evaporation to be maintained. This is a continual process occurring throughout the life cycle, ensuring that regions of positive latent heat flux never become saturated and regions of frictional divergence never dry out.

Since the divergence term (Figure 8b) cannot produce net moisture transport out of the boundary layer, this moisture must converge elsewhere in the cyclone-wave boundary layer. The convergence, forced by surface drag and large-scale ageostrophic flow, occurs in the footprint of the warm-conveyor belt. This leads to a large build-up of moisture in the WCB region, resulting in the saturated boundary layer discussed in Section 4. Some moisture is returned to the surface via latent heat exchange, but the
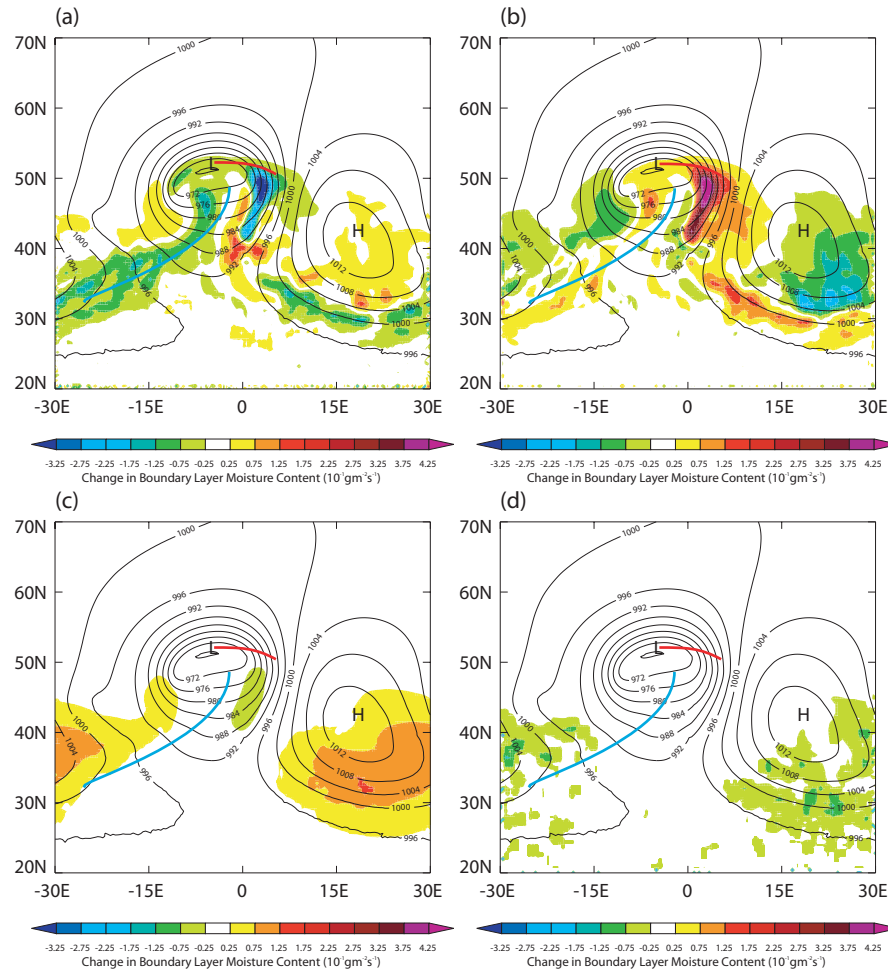
Fig. 8 Tendencies in boundary-layer moisture content (coloured) at day 7 due to various terms in Equation 9. (a) Advection across the boundary-layer top (term 2); (b) horizontal divergence within the boundary layer (term 3); (c) net vertical transport by boundary-layer turbulence (term 4); and, (d) transport by shallow convection $((\rho q w)_{conv})$. The pressure at mean sea level is overplotted (contoured, interval 4 hPa).

majority of this moisture is loaded onto the warm-conveyor belt and ventilated from the boundary layer by large-scale ascent (Figure 8a).

Warm-conveyor belts are almost 100 % efficient at converting moisture into precipitation (Eckhardt et al., 2004), and hence most of this moisture loaded onto the WCB will ultimately return to the surface as precipitation. This completes a cycle of moisture transport from the surface to the troposphere and back, forced by the cyclone wave and mediated by the boundary-layer dynamics. However, it is noticeable from Figures 3a and 4b that the surface precipitation from the WCB is in a very different location to the surface evaporation, showing how the cyclone wave and boundary

layer act together to transport moisture large distances, both in the east-west and north-south directions.

Within the anticyclonic region, large-scale subsidence moves some moisture from the free troposphere into the boundary layer. However, this term (Figure 8a) is small compared to the evaporation term (Figure 8c), which leads to a major difference between the moisture budget and the mass budget, which was considered by Sinclair et al. (2010). Large-scale subsidence is a major source of mass flow into the boundary layer, but this is not the case for moisture since the subsiding air tends to be much dryer. There is also some ventilation noticeable south of the low centre and wrapping westwards around the south of the high pressure region. This is matched by convergence, as shown in Figure 8b, and is associated with the cold front, which at this stage is intensifying and starting to form a long, trailing front that almost wraps around the entire domain. The convergence of air forming the front is also responsible for moisture convergence and ventilation through frontal ascent. Ventilation appears enhanced directly south of the low centre due to sharp gradients in h near the cold front, so that there is a tendency for the boundary layer to be ventilated via frontal outflow. However, term 1 in Equation 9 acts to balance this frontal outflow, since at a fixed point in space, the boundary layer is growing in time as the front passes over it.

The other major difference to the dry simulations is the transport of moisture by shallow convection (Figure 8d). Whilst the strongest ventilation of moisture is on the warm-conveyor belt, the large area over which shallow convection occurs means that the total, domain-integrated, moisture ventilated by the two processes is comparable. At the time shown (day 7), moisture is being ventilated at a rate of 3.1×10^8 kg s^{-1} by large-scale advection (i.e., due to term 2, as in Figure 8a), compared with 3.5×10^8 kg s^{-1} by shallow convection (i.e., due to $(\rho q w)_{\text{conv}}$, as in Figure 8d). Indeed, the two processes are of comparable importance throughout much of the life cycle, albeit with shallow convection triggered slightly earlier in the life cycle and with the large-scale moisture flux becoming the stronger process as the cyclone-wave intensifies. Gutowski and Jiang (1998) discussed how moisture introduced into the troposphere at the shallow convective cloud tops can be advected eastwards and polewards by the cyclone wave. However, unlike the warm-conveyor belt flow, this moisture flow does not ascend, but rather remains between 3 and 4 km for several days, before converging in the region of the cold front.

7 Conclusions

We have investigated the boundary-layer structure that evolves under a developing mid-latitude cyclone wave, with the aim of expanding conceptual models of dry boundary layers on this scale. Locally and instantaneously, the structures observed mirror closely textbook boundary-layer types. In post-frontal and high-pressure regions, the evolution is analogous to daytime convective boundary-layer growth, with a single mixed layer growing past the lifting-condensation-level, capping stratocumulus becoming decoupled from the surface and cumulus convection initiated beneath it. Within the warm sector, the evolution is more typical of a nocturnal boundary layer, with a stable profile, low-level cloud or fog formation, and dew condensing out onto

the surface. These two extremes are also linked by transitional regions as the cyclone wave progresses.

The inclusion of moisture introduces an extra aspect for the conceptual boundary-layer structures formed, and the quantity D^* allows further classification of three boundary-layer moisture regimes. Low, positive D^* corresponds to the bottom-up, moistening, boundary layer, which can evolve to support cumulus convection above. High, positive D^* corresponds to the top-down, entrainment-drying boundary layer, which results in cloud-free air or thin stratocumulus. Negative D^* corresponds to a boundary layer losing moisture to the surface.

However, these processes are fundamentally different from the traditional "single-column" view of boundary layers. The regimes are not forced by solar heating and the local surface energy balance, but rather by large-scale thermal advection by the synoptic system. It is this synoptic-scale forcing that maintains the structure of the boundary layer over large areas. The character of this forcing also creates subtle differences in the profiles. The warm-conveyor belt boundary layer, for example, departs in some important ways from the classical nocturnal boundary layer, containing Lagrangian, three-dimensional features. Moisture advection, cloud formation and precipitation all contribute to a well-mixed moisture profile throughout a large depth of the atmosphere, in a region that is stable on buoyancy grounds. This highlights the importance of considering the full three-dimensional structure of the boundary layer in cases where horizontal divergence is large.

Through the use of a boundary-layer moisture budget, we have been able to quantify how moisture is moved within and ventilated from the boundary layer. There are two main pathways through which moisture is ventilated, and these are shown schematically in Figure 9. The warm-conveyor belt ventilates moisture in much the
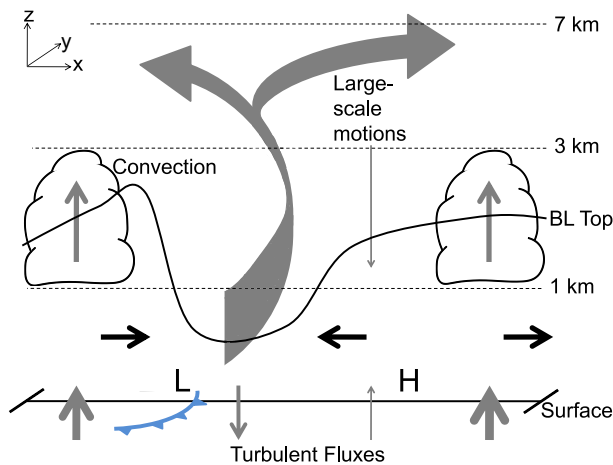

Fig. 9 Schematic representing the flows of moisture within the cyclone boundary layer, grey arrows representing sources and sinks of boundary-layer moisture and black arrows representing movement within the boundary layer. The arrow thickness provides a qualitative indication of the relative strength of the various flows. L and H denote the low and high pressure centres respectively, with the cold front marked in blue. The approximate height of features is marked, along with the height of the boundary layer.

same way as it does mass (Sinclair et al., 2010), with the moisture source being provided by convergence within the boundary layer. However shallow convection has been demonstrated to be an equally efficient mechanism of ventilating moisture into the free troposphere.

The importance of warm-conveyor belts for moisture transport and precipitation events is well documented (Eckhardt et al., 2004; Field and Wood, 2007), but until now the importance of boundary-layer processes has not been recognised. The moisture budget considered here has enabled us to uncover how long-range transport within the boundary layer leads to this moisture convergence under the WCB region. The moisture is evaporated far from the WCB region, into the post frontal and anticyclonic boundary layer, where the latent heat flux is large and positive. It is then transported by divergent motions that are forced by surface drag and ageostrophic flow, ultimately converging under the warm-conveyor belt source.

A key difference between moisture and some other variables, such as mass or heat, is that moisture flux is almost always directed upwards at the boundary-layer top. In the convective boundary-layer regime, heat and mass are moved into the boundary layer by large-scale subsidence. Although large-scale subsidence does move a small amount of moisture into the boundary layer, in these cyclone waves it is typically co-located with shallow convection, which acts to maintain a net flux of moisture out of the boundary layer. This ventilation mechanism will also have consequences for pollutant transport out of the boundary layer. Sinclair et al. (2008) discussed how dry cyclone waves can remove pollutants from the boundary layer on the WCB, but this study has shown that shallow convection would be expected to increase the ventilation rate.

Figure 9 shows how moisture is continually being redistributed within the cyclone wave so that there are no locations where the boundary layer is strongly moistening or drying. This again demonstrates the importance of examining the three-dimensional boundary-layer structure, since the simple D^* measure cannot account for this continual transport. Evaporation acts to moisten post-frontal and high-pressure regions, while divergence and convection act to dry these regions. By contrast, convergence acts to moisten the low-pressure regions, whilst condensation and large-scale ascent act to dry these regions. Large-scale motions outside the boundary layer act to move the moisture ventilated eastwards and northwards, eventually returning it to the surface as precipitation great distances from where it was originally evaporated.

Other processes not included in this study will also affect the boundary-layer structure. Whilst the diurnal cycle is small over the ocean, cloud-radiation feedbacks will affect the observed cloud structure. If we had included radiation in the simulations, we would expect to find a de-stabilising effect on the atmosphere, reducing the size of the stable areas and increasing the extent of the convective boundary layer. Boutle et al. (2007) also demonstrated the large effect that variations in sea-surface temperature can have on surface fluxes. However, comparison to case studies (e.g. Neiman et al., 1990; Brown et al., 2008) demonstrates that the results presented here are certainly realistic and any such uncertainties would appear most unlikely to affect the qualitative conclusions that have been drawn. Moreover, the techniques employed could be applied to simulations of real cases in order to study the mid-latitude water cycle. Latent heat released from warm-conveyor belt rain has a large affect on cyclone

development, and cyclone waves provide the major engine for poleward transport of heat and moisture. Hence the understanding obtained here of how tropospheric moisture is connected to its oceanic source, and how the moisture evolution is mediated by boundary-layer dynamics, has important consequences for weather and climate studies.

Appendix

We outline the derivation of Equation 9, proceeding from a volume integral of Equation 8. The first term from the left-hand side of Equation 8 can be simplified using the Leibniz rule:

$$\int_A \int_0^h \frac{\partial}{\partial t}(\rho q) dz dA = \int_A \left[\frac{\partial}{\partial t}\left(\int_0^h \rho q dz \right) - (\rho q)_h \frac{\partial h}{\partial t} \right] dA. \tag{10}$$

The second term from the left-hand side of Equation 8 requires the use of the divergence theorem:

$$\int_A \int_0^h \nabla.(\rho q \mathbf{u}) dz dA = \int_S \rho q \mathbf{u}.\mathbf{n} dS, \tag{11}$$

where S is the surface enclosing the boundary-layer control volume and $\mathbf{n}$ is the unit normal to this. Since we have already Reynolds averaged, there is no mean flow through the bottom surface and we can separate the surface integral into contributions from the sides ($B \times h$, where B is the boundary to A) and top (T) of our control volume:

$$\int_S \rho q \mathbf{u}.\mathbf{n} dS = \int_B \int_0^h \rho q \mathbf{v}.\mathbf{n} dz dB + \int_T (\rho q)_h \mathbf{u}.\mathbf{n} dT. \tag{12}$$

Since the boundary-layer top can slope in x and y, the area element $dT \neq dA$, but rather they are related by

$$dT = \sqrt{1 + \left(\frac{\partial h}{\partial x} \right)^2 + \left(\frac{\partial h}{\partial y} \right)^2} dA, \tag{13}$$

and using this relation and the divergence theorem in two dimensions we obtain

$$\int_A \int_0^h \nabla.(\rho q \mathbf{u}) dz dA = \int_A \left[\nabla_2.\left(\int_0^h \rho q \mathbf{v} dz \right) + (\rho q)_h \mathbf{u}.\tilde{\mathbf{n}} \right] dA, \tag{14}$$

where $\tilde{\mathbf{n}} = \mathbf{n}\sqrt{1 + \left(\frac{\partial h}{\partial x} \right)^2 + \left(\frac{\partial h}{\partial y} \right)^2}$. Finally, the terms on the right-hand side of Equation 8 are volume-integrated thus:

$$\int_A \int_0^h \left[-\frac{\partial}{\partial z}(\rho \overline{w'q'}) + \mathscr{S} \right] dz dA = \int_A \left[-(\rho \overline{w'q'})_h + (\rho \overline{w'q'})_0 + \int_0^h \mathscr{S} dz \right] dA. \tag{15}$$

Combining Equations 10, 14 and 15 and dropping the integration over the arbitrary area A, we obtain Equation 9.

References

Adamson DS, Belcher SE, Hoskins BJ, Plant RS (2006) Boundary-layer friction in midlatitude cyclones. Q J Roy Meteorol Soc 132:101–124

Balasubramanian G, Garner ST (1997) The Role of Momentum Fluxes in Shaping the Life Cycle of a Baroclinic Wave. J Atmos Sci 54:510–533

Beare RJ (2007) Boundary layer mechanisms in extratropical cyclones. Q J Roy Meteorol Soc 133:503–515

Beare RJ, MacVean MK (2004) Resolution sensitivity and scaling of large-eddy simulations of the stable boundary layer. Boundary-Layer Meteorol 112:257–281

Becker A, Kraus H, Ewenz CM (1996) Frontal substructures within the planetary boundary layer. Boundary-Layer Meteorol 78:165–190

Beljaars ACM, Holtslag AAM (1991) Flux parameterization over land surfaces for atmospheric models. J Appl Meteorol 30:327–341

Berger BW, Friehe CA (1995) Boundary-layer structure near the cold front of a marine cyclone during "ERICA". Boundary-Layer Meteorol 73:227–253

Boutle IA, Beare RJ, Belcher SE, Plant RS (2007) A note on boundary-layer friction in baroclinic cyclones. Q J Roy Meteorol Soc 133:2137–2141

Brown AR, Beare RJ, Edwards JM, Lock AP, Keogh SJ, Milton SF, Walters DN (2008) Upgrades to the boundary-layer scheme in the Met Office numerical weather prediction model. Boundary-Layer Meteorol 128:117–132

Browning KA (1990) Organization of clouds and precipitation in extratropical cyclones. In: Extratropical Cyclones: The Erik Palmén Memorial Volume, Amer. Meteorol. Soc., Boston, pp 129–153

Businger JA, Charnock H (1983) Boundary layer structure in relation to larger-scale flow: Some remarks on the JASIN observations. Phil Trans Roy Soc Lond A 308:445–449

Eady ET (1949) Long waves and cyclone waves. Tellus 1:33–52

Eckhardt S, Stohl A, Wernli H, James P, Forster C, Spichtinger N (2004) A 15-year climatology of warm conveyor belts. J Climate 17:218–237

Emanuel K, Fantini M, Thorpe A (1987) Baroclinic instability in an environment of small stability to slantwise moist convection. Part I: Two-dimensional models. J Atmos Sci 44:1559–1573

Field PR, Wood R (2007) Precipitation and Cloud Structure in Midlatitude Cyclones. J Climate 20:233–254

Gutowski WJ, Jiang W (1998) Surface-flux regulation of the coupling between cumulus convection and baroclinic waves. J Atmos Sci 55:940–953

Gutowski WJ, Branscome LE, Stewart DA (1992) Life cycles of moist baroclinic eddies. J Atmos Sci 49:306–319

Kuo YH, Reed RJ, Low-Nam S (1991) Effects of Surface Energy Fluxes during the Early Development and Rapid Intensification Stages of Seven Explosive Cyclones in the Western Atlantic. Mon Weather Rev 119:457–476

Levy G (1989) Surface dynamics of observed maritime fronts. J Atmos Sci 46:1219–1232

Lock AP, Brown AR, Bush MR, Martin GM, Smith RNB (2000) A New Boundary Layer Mixing Scheme. Part I: Scheme Description and Single-Column Model

Tests. Mon Weather Rev 128:3187–3199

Mahrt L (1991) Boundary-layer moisture regimes. Q J Roy Meteorol Soc 117:151–176

Martin GM, Ringer MA, Pope V, Jones A, Dearden C, Hinton T (2006) The Physical Properties of the Atmosphere in the New Hadley Centre Global Environment Model (HadGEM1). Part I: Model Description and Global Climatology. J Climate 19:1274–1301

Neiman PJ, Shapiro MA, Donall EG, Kreitzberg CW (1990) Diabatic Modification of an Extratropical Marine Cyclone Warm Sector by Cold Underlying Water. Mon Weather Rev 118:1576–1590

Nuss WA (1989) Air-sea interaction influences on the structure and intensification of an idealized marine cyclone. Mon Weather Rev 117:351–369

Pavan V, Hall N, Valdes P, Blackburn M (1999) The importance of moisture distribution for the growth and energetics of mid-latitude systems. Ann Geophys 17:242–256

Polvani LM, Esler JG (2007) Transport and mixing of chemical airmasses in idealized baroclinic life cycles. J Geophys Res 112:D23,102

Sinclair VA, Gray SL, Belcher SE (2008) Boundary-layer ventilation by baroclinic life cycles. Q J Roy Meteorol Soc 134:1409–1424

Sinclair VA, Belcher SE, Gray SL (2010) Synoptic controls on boundary-layer structure. Boundary-Layer Meteorol In Press

Taylor PK, Guymer TH (1983) The structure of an atmospheric warm front and its interaction with the boundary layer. Phil Trans Roy Soc Lond A 308:341–358

Thorncroft CD, Hoskins BJ, McIntyre ME (1993) Two paradigms of baroclinic-wave life-cycle behaviour. Q J Roy Meteorol Soc 119:17–55

Troen I, Mahrt L (1986) A simple model of the atmospheric boundary layer; sensitivity to surface evaporation. Boundary-Layer Meteorol 37:129–148

Wernli H, Fehlmann R, Lüthi D (1998) The effect of barotropic shear on upper-level induced cyclogenesis: Semigeostrophic and primitive equation numerical simulations. J Atmos Sci 55:2080–2094